Estimating Rotation Speed on the Sphere: Low-Rank Fokker–Planck Prediction on $\mathbb{S}^2 \times \mathbb{R}$

Daniel Frisch and Uwe D. Hanebeck

***Abstract*— We derive a low-rank Fokker–Planck (FP) predictor for stochastic dynamics on the Riemannian manifold $\mathbb{S}^2 \times \mathbb{R}$. This three-dimensional state space combines a pointing direction on $\mathbb{S}^2$ that is rotating about a fixed axis with the angular velocity defined on $\mathbb{R}$. Using a constant-velocity-like system model, the rotation speed can be inferred from directional measurements alone. Despite its seemingly simple dynamics, the curvature and periodicity of $\mathbb{S}^2$ make this an inherently nonlinear estimation problem. We represent the spherical part as an equal-area grid with equidistant height $u = \cos\theta$ and azimuth φ discretization. The full grid is formed via a Cartesian product combining this with an equidistant velocity vector. The discretized prediction operator is a sum of Kronecker products, which lets us propagate the joint density entirely in a compressed canonical polyadic tensor format – using operator splitting for the time step and alternating least squares (ALS) for the rank truncation – without ever forming the full grid. On a bimodal angular-speed scenario with about a million grid points, the predictor matches dense reference solvers to high accuracy at an order-of-magnitude lower runtime, and its advantage grows as the grid is refined. It can be used, e.g., for spin-state estimation of uncooperative space objects or state estimation of a pan-tilt radar antenna.**

I. Introduction

Many estimation problems consider a rotating object whose orientation can be summarized by a single pointing direction, a boresight or body axis, that sweeps along a circle on the unit sphere $\mathbb{S}^2$ as the object spins about a fixed axis at some angular speed ω. Often this spin rate is itself unknown and must be inferred from noisy observations of the pointing direction alone, see Fig. 1a. A prototypical example is the spin-state estimation of a tumbling, uncooperative space object such as a piece of orbital debris or a defunct satellite [1], [2]: a sensor observes only sparse optical line-of-sight or photometric data, from which both the current pointing direction on $\mathbb{S}^2$ and the unknown spin rate on $\mathbb{R}$ must be recovered jointly. The curvature and periodicity of the sphere turn even this seemingly simple constant-speed rotation into an inherently nonlinear estimation problem.

Estimating such rotational states calls for a probability density representation on a curved, periodic domain – one that is at once expressive enough to capture the (potentially multimodal) uncertainty and structured enough to admit prediction and filtering at a manageable computational cost.

Classical assumed-density filters fix a parametric family, most prominently the Gaussian, and propagate only its parameters, ideally with carefully placed deterministic samples [3], [4], [5] maximizing the update accuracy. Gaussian mixtures [6], [7] add flexibility, but at a quickly growing cost.

Daniel Frisch and Uwe D. Hanebeck are with the Intelligent Sensor-Actuator-Systems Laboratory (ISAS), Institute for Anthropomatics and Robotics, Karlsruhe Institute of Technology (KIT), Germany (e-mail: daniel.frisch@kit.edu; uwe.hanebeck@kit.edu).

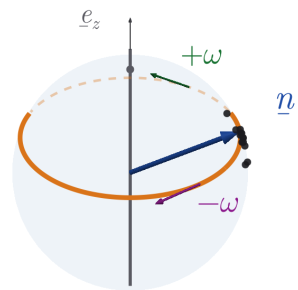

(a) Application scenario: a boresight axis $\underline{n} \in \mathbb{S}^2$ (blue vector) rotates about the vertical spin axis $\underline{e}_z$ at unknown, nearly constant speed $\omega \in \mathbb{R}$, tracing a circle of nearly constant $u = \cos\theta$ (orange). The ambiguous spin sense $+\omega_0$ (green) vs. $-\omega_0$ (purple) makes the estimate bimodal, and only noisy directional measurements of $\underline{n}$ (black dots) are available.

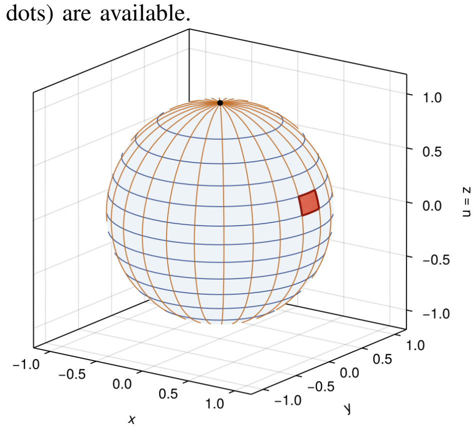

(b) Equal-area (u, φ) discretization of $\mathbb{S}^2$: parallels of constant u (blue) and meridians of constant φ (orange) bound the cell-centered grid, one cell highlighted (red). Uniform spacing in $u = \cos\theta$ makes every cell carry the same surface area $\Delta_u \Delta_\varphi$, so the cells grow zonally wider near the equator and meridionally coarser near the poles.

Fig. 1: The estimation problem on $\mathbb{S}^2 \times \mathbb{R}$ (a) and the equal-area grid (spherical part only) used to represent densities on it (b).

On curved and periodic manifolds, however, probability mass transported away in one direction eventually "comes back from the other side," see Fig. 2, so that even a constant-velocity motion turns inherently nonlinear. Manifold-aware filters have therefore been devised specifically for the circle $\mathbb{S}^1$ [8], the sphere $\mathbb{S}^2$ [9], [10], [11], [12], [13], the torus $\mathbb{T}^2$ [14], [15], [16], and the rigid-body groups SE(2) [17], [18] and SE(3) [19], [20], [21]. Most of these are Linear

Regression Kalman filter (LRKF)-type filters that are limited by linearization in the joint measurement and state space. A purely sample-based representation by a point cloud is an alternative, but its Bayesian update is prone to degeneracy and only partially remedied by progressive and deterministic resampling [22], [23], or at rather high cost with Newton-flow transport [24], [25], [26].

A. Grid-Based Low-Rank Representation

A more direct representation discretizes the relevant part of the state space on a regular grid, which renders the measurement update trivial and concentrates the effort in the prediction step, i.e., the solution of the Fokker-Planck (FP) equation [27], [28], [29]. On periodic manifolds this prediction can be carried out efficiently in the Fourier domain [30], [31], as demonstrated on the torus [32], the sphere [33], [34], and the groups $\mathrm{SO}(2)$ [35], [36] and $\mathrm{SE}(3)$ [37]. All grid-based methods, however, share the curse of dimensionality, as the number of stored probability values grows exponentially with the state-space dimension. Much of this growth can be tamed because the probability tensor is typically highly compressible by CANDECOMP/PARAFAC (CP) low-rank tensor decompositions [38], [39], which generalize the truncated singular value decomposition of the two-dimensional (2D) case to a sum of a few rank-one tensors in three or more dimensions, such as the $\mathbb{S}^2 \times \mathbb{R}$ domain considered here. Prediction and filtering can then be performed directly on this compressed representation, without ever expanding the full grid [40], [41], [42], [43], [44].

B. Contribution

Building on the cylinder-based low-rank FP predictor of [45], we extend the tensorized prediction to the sphere, i.e., the product manifold $\mathbb{S}^2 \times \mathbb{R}$. The directional part $\underline{n} \in \mathbb{S}^2$ models a pointing direction or boresight axis, while the real component $\omega \in \mathbb{R}$ is its unknown angular speed of rotation about a fixed axis, so that the rotation speed can be inferred from directional measurements – the spherical counterpart of estimating a shaft speed from an angular encoder. Compared with the cylinder, the directional state now lives on a curved, two-dimensional manifold, which replaces the plain periodic diffusion by the spherical Laplace-Beltrami operator and turns the matrix-shaped density into a three-way tensor that we compress with a canonical polyadic decomposition. Closed directional manifolds are, in fact, particularly well suited to grid-based representations [33], [34]: their bounded extent means that only the grid resolution has to be chosen rather than an artificial truncation of the domain, so that here only the unbounded angular-speed axis ω requires a finite cutoff.

II. Directional Estimation on $\mathbb{S}^2 \times \mathbb{R}$

A. System Dynamics

We consider a stochastic process on the product manifold

$$\underline{x} = (\underline{n}, \omega) \in \mathbb{S}^2 \times \mathbb{R} \ , \tag{1}$$

where $\underline{n} \in \mathbb{S}^2 \subset \mathbb{R}^3$ represents a pointing direction (boresight axis) and $\omega \in \mathbb{R}$ is the angular speed of its rotation. Estimating both jointly is the direct sphere-analog of the rotating-shaft scenario considered in [45], where the cylinder coordinate φ played the role of $\underline{n}$ and ω was likewise an unobserved state component to be inferred from angular measurements. We parametrize $\mathbb{S}^2$ by the cylindrical coordinates

$$\underline{n}(u, \varphi) = \begin{bmatrix} \sqrt{1-u^2}\,\cos\varphi \\ \sqrt{1-u^2}\,\sin\varphi \\ u \end{bmatrix} \ , \tag{2}$$

where $u = \cos\theta \in [-1, 1]$ is the height above the equator (the cosine of the colatitude θ) and $\varphi \in \mathbb{S} = \mathbb{R}/(2\pi\mathbb{Z})$ is the azimuth (where / denotes the quotient space). The full state is then $\underline{x} = (u, \varphi, \omega) \in [-1, 1] \times \mathbb{S} \times \mathbb{R}$. The motivation for using $u = \cos\theta$ instead of θ itself is that the surface measure on $\mathbb{S}^2$ becomes uniform, $\mathrm{d}A = \mathrm{d}u\,\mathrm{d}\varphi$, removing the $\sin\theta$ Jacobian that otherwise causes a coordinate singularity at the poles. It converts the spherical Laplace-Beltrami operator into a regular Sturm-Liouville problem in the latitude variable, with diffusion coefficient $a(u) = (1-u^2)$ vanishing smoothly at $u = \pm 1$. As the simplest non-trivial dynamical system on $\mathbb{S}^2 \times \mathbb{R}$, we consider rotation of $\underline{n}$ about a known fixed axis – without loss of generality the z-axis – at unknown angular speed ω, perturbed by isotropic Brownian motion on the sphere, while ω itself follows a Wiener process, i.e., nearly constant angular speed. The corresponding stochastic differential equation in Stratonovich form reads

$$\mathrm{d}\underline{n} = (\underline{e}_z \times \underline{n})\omega\,\mathrm{d}t + q_n \sum_{k=1}^{2} (\underline{e}_k(\underline{n}) \times \underline{n}) \circ \mathrm{d}w_k \ , \tag{3}$$

$$\mathrm{d}\omega = q_\omega\,\mathrm{d}w_3 \ , \tag{4}$$

where $\underline{e}_z = [0, 0, 1]^\top$ is the rotation axis, "$\times$" denotes the cross product in $\mathbb{R}^3$, $(\underline{e}_1(\underline{n}), \underline{e}_2(\underline{n}))$ is any orthonormal frame of the tangent space $T_{\underline{n}}\mathbb{S}^2$, w_1, w_2, w_3 are independent standard Wiener processes, and q_n, q_ω are infinitesimal noise intensities. The symbol "$\circ$" denotes the Stratonovich interpretation of the stochastic integral, which we use because for state-dependent diffusion coefficients on a manifold it preserves the constraint $\|\underline{n}\|_2 = 1$ under the ordinary chain rule and yields the Laplace-Beltrami operator as the infinitesimal generator without additional drift correction terms [46]. The deterministic drift transports probability mass along circles of constant u, with the transport speed determined by the current value of ω. The stochastic part on $\underline{n}$ is the isotropic Wiener process on $\mathbb{S}^2$, whose infinitesimal generator is the Laplace-Beltrami operator $\Delta_{\mathbb{S}^2}$; the stochastic part on ω is the standard one-dimensional Wiener process. The corresponding FP equation for the time evolution of the joint probability density $p(u, \varphi, \omega, t)$ is

$$\frac{\partial p}{\partial t} = -\omega \frac{\partial p}{\partial \varphi} + \frac{q_n^2}{2}\,\Delta_{\mathbb{S}^2}\, p + \frac{q_\omega^2}{2}\,\frac{\partial^2 p}{\partial \omega^2} \ , \tag{5}$$

with the Laplace-Beltrami operator on $\mathbb{S}^2$ in the (u, φ) chart

$$\Delta_{\mathbb{S}^2}\, p = \frac{\partial}{\partial u}\left((1-u^2)\frac{\partial p}{\partial u}\right) + \frac{1}{1-u^2}\,\frac{\partial^2 p}{\partial \varphi^2} \ . \tag{6}$$

The first term in (5) describes the ω-dependent transport along the periodic φ direction, the spherical diffusion term causes "broadening" of the marginal density across the sphere, and the last term diffuses the marginal density along the unbounded ω axis. Thereby the uncertainty in ω induces additional blurring in φ. Even though the drift is linear in ω, the problem is inherently nonlinear due to the curvature and periodicity of $\mathbb{S}^2$. Summarizing, as opposed to particle filters, where prediction is performed with a selection of samples, the entire probability density is propagated in continuous time.

Note that $u = \pm 1$ are coordinate poles, not physical boundaries. The factor $(1-u^2)$ multiplying the radial flux in (6) vanishes at the poles, automatically enforcing the correct no-flux behavior, so no boundary conditions need to be imposed by hand. The factor $1/(1-u^2)$ in the azimuthal term is harmless on a grid that does not place nodes at $u = \pm 1$, and is moreover compensated by $\partial^2 p/\partial\varphi^2 \to 0$ as $u \to \pm 1$, since smooth functions on $\mathbb{S}^2$ are constant in φ at the poles.

B. State Space Discretization

The probability density is represented as a third-order tensor $\mathbf{P} \in \mathbb{R}^{N_\varphi \times N_u \times N_\omega}$, whose entry $\mathbf{P}_{ijm}$ corresponds to the grid point $(\varphi_i, u_j, \omega_m)$. We use column-major linear indexing $\underline{p} \in \mathbb{R}^{N_\varphi N_u N_\omega}$ via $k = i + (j-1)N_\varphi + (m-1)N_\varphi N_u$, with φ as the fastest and ω as the slowest index.

We discretize the state space using a regular grid representation. For the periodic azimuth φ we use N_φ uniformly spaced points on $\mathbb{S}$, for the latitudinal coordinate $u \in [-1, 1]$ we use a *cell-centered* grid with N_u points, and for the angular speed $\omega \in [\omega_{\min}, \omega_{\max}]$ we use a vertex-centered grid with N_ω points,

$$\varphi_i = (i-1) \cdot \Delta_\varphi \ , \tag{7}$$

$$u_j = -1 + \tfrac{2j-1}{2} \cdot \Delta_u \ , \tag{8}$$

$$\omega_m = \omega_{\min} + (m-1) \cdot \Delta_\omega \ , \tag{9}$$

for $i \in \{1, \dots, N_\varphi\}$, $j \in \{1, \dots, N_u\}$, $m \in \{1, \dots, N_\omega\}$, with grid spacings

$$\Delta_\varphi = \frac{2\pi}{N_\varphi} \ , \quad \Delta_u = \frac{2}{N_u} \ , \quad \Delta_\omega = \frac{\omega_{\max} - \omega_{\min}}{N_\omega - 1} \ . \tag{10}$$

See Fig. 1b for a visualization of the spherical part. The cell-centered placement in u avoids evaluating any quantity at the coordinate poles $u = \pm 1$, where $1/(1-u^2)$ would diverge. A uniform grid in $u = \cos\theta$ is equivalent to an equal-area tessellation of $\mathbb{S}^2$ (since $\mathrm{d}A = \mathrm{d}u\,\mathrm{d}\varphi$), see Fig. 1b, so each tensor entry $\mathbf{P}_{ijm}$ corresponds to the same surface area and hence the same nominal probability mass without any Jacobian reweighting. Geometrically, this makes the cells anisotropic near the poles: the meridional arc length $\mathrm{d}s_\theta = \mathrm{d}u/\sqrt{1-u^2}$ becomes coarser, while the zonal arc length $\mathrm{d}s_\varphi = \sqrt{1-u^2}\,\mathrm{d}\varphi$ becomes finer, but the smoothness constraint that any density on $\mathbb{S}^2$ must be φ-independent at the poles prevents the polar cells from carrying genuine azimuthal structure. Combined with the $(1-u^2)$ factor in the radial flux, which suppresses transport near the poles, this anisotropy is benign for the diffusion-dominated dynamics considered here.

C. Fokker–Planck Equation Discretization

The discretized FP equation takes the form

$$\frac{\partial \underline{p}}{\partial t} = \mathbb{L}\,\underline{p} \ , \tag{11}$$

with the FP operator $\mathbb{L}$. With the chosen index ordering, $\mathbb{L}$ decomposes into four three-fold Kronecker products,

$$
\begin{aligned}
\mathbb{L} &= \mathbb{L}_1 + \mathbb{L}_2 + \mathbb{L}_3 + \mathbb{L}_4 && (12)\\
&= -\operatorname{diag}(\underline{\omega}) \otimes \mathbf{I}(N_u) \otimes \mathbf{D}_\varphi && (13)\\
&\quad + \tfrac{q_n^2}{2}\,\mathbf{I}(N_\omega) \otimes \mathbf{D}_u \otimes \mathbf{I}(N_\varphi) && (14)\\
&\quad + \tfrac{q_n^2}{2}\,\mathbf{I}(N_\omega) \otimes \operatorname{diag}\!\Big(\tfrac{1}{1-\underline{u}^2}\Big) \otimes \mathbf{D}_{\varphi\varphi} && (15)\\
&\quad + \tfrac{q_\omega^2}{2}\,\mathbf{D}_{\omega\omega} \otimes \mathbf{I}(N_u) \otimes \mathbf{I}(N_\varphi) && (16)\\
&= \sum_{k=1}^{4} \mathbf{A}_{\omega,k} \otimes \mathbf{A}_{u,k} \otimes \mathbf{A}_{\varphi,k} \ , && (17)
\end{aligned}
$$

where $\operatorname{diag}(\underline{\omega})$ is the diagonal matrix of grid values ω_m, and $\operatorname{diag}\big(1/(1-\underline{u}^2)\big)$ is the diagonal matrix with entries $1/(1-u_j^2)$. As in the cylinder case [45], the angular speed ω is again a state component, so the drift contribution $\mathbb{L}_1$ takes the same Kronecker structure $-\operatorname{diag}(\underline{\omega}) \otimes (\cdots) \otimes \mathbf{D}_\varphi$ as in [45, Eq. 9], with the trivial $\mathbf{I}(N_u)$ in the middle factor reflecting that the drift is independent of u. The periodic first-difference matrix $\mathbf{D}_\varphi$ on $\mathbb{S}$ is identical to [45, Eq. 10],

$$\mathbf{D}_\varphi = \frac{1}{2\Delta_\varphi} \begin{bmatrix} 0 & 1 & 0 & 0 & 0 & -1 \\ -1 & 0 & 1 & 0 & 0 & 0 \\ 0 & -1 & 0 & 1 & 0 & 0 \\ 0 & 0 & \ddots & \ddots & \ddots & 0 \\ 0 & 0 & 0 & -1 & 0 & 1 \\ 1 & 0 & 0 & 0 & -1 & 0 \end{bmatrix} \ . \tag{18}$$

The radial diffusion matrix $\mathbf{D}_u \in \mathbb{R}^{N_u \times N_u}$ in $\mathbb{L}_2$ discretizes the conservative Sturm-Liouville operator $\partial_u\big((1-u^2)\partial_u p\big)$ on the cell-centered u-grid. Defining the cell faces (separation points between cells) $u_{j-\frac{1}{2}} = -1 + (j-1)\Delta_u$, for $j = 1, \dots, N_u + 1$, we use the standard two-point flux

$$F_{j-\frac{1}{2}} = \Big(1 - u_{j-\frac{1}{2}}^2\Big) \cdot \frac{p_j - p_{j-1}}{\Delta_u} \ , \tag{19}$$

yielding the symmetric tridiagonal matrix with entries

$$
\begin{aligned}
&[\mathbf{D}_u]_{j,j-1} = \frac{1 - u_{j-\frac{1}{2}}^2}{\Delta_u^2} \ , \quad [\mathbf{D}_u]_{j,j+1} = \frac{1 - u_{j+\frac{1}{2}}^2}{\Delta_u^2} \ , \\
&[\mathbf{D}_u]_{j,j} = -\frac{\Big(1 - u_{j-\frac{1}{2}}^2\Big) + \Big(1 - u_{j+\frac{1}{2}}^2\Big)}{\Delta_u^2} \ ,
\end{aligned} \tag{20}
$$

and zeros elsewhere, for $j = 1, \dots, N_u$. In the first and last rows, the boundary face coefficients $1 - u_{\frac{1}{2}}^2 = 1 - u_{N_u+\frac{1}{2}}^2 = 0$ vanish (since $u_{\frac{1}{2}} = -1$ and $u_{N_u+\frac{1}{2}} = +1$), so the would-be off-grid entries $[\mathbf{D}_u]_{1,0}$ and $[\mathbf{D}_u]_{N_u,N_u+1}$ drop out automatically without any explicit boundary condition, and the diagonal entries reduce to $[\mathbf{D}_u]_{1,1} = -(1 - u_{\frac{3}{2}}^2)/\Delta_u^2$ and $[\mathbf{D}_u]_{N_u,N_u} = -(1 - u_{N_u-\frac{1}{2}}^2)/\Delta_u^2$. The matrix $\mathbf{D}_u$ is symmetric negative-semidefinite.

The azimuthal second-difference matrix $\mathbf{D}_{\varphi\varphi} \in \mathbb{R}^{N_\varphi \times N_\varphi}$ in $\mathbb{L}_3$ is the periodic analog of the second-derivative finite-difference matrix,

$$\mathbf{D}_{\varphi\varphi} = \frac{1}{\Delta_\varphi^2} \begin{bmatrix} -2 & 1 & 0 & 0 & 0 & 1 \\ 1 & -2 & 1 & 0 & 0 & 0 \\ 0 & 1 & -2 & 1 & 0 & 0 \\ 0 & 0 & \ddots & \ddots & \ddots & 0 \\ 0 & 0 & 0 & 1 & -2 & 1 \\ 1 & 0 & 0 & 0 & 1 & -2 \end{bmatrix} , \tag{21}$$

where the 1 entries in the upper-right and lower-left corners again account for periodicity.

The coefficient $1/(1-u^2)$ in $\mathbb{L}_3$ is bounded on the cell-centered grid, but grows like $1/\Delta_u$ at the polar rings $j \in \{1, N_u\}$. While this is harmless for the dense reference operator – the smoothness constraint on $\mathbb{S}^2$ forces $\mathbf{D}_{\varphi\varphi}\, \underline{p} \to 0$ at the poles so the product remains finite – it does inflate the spectral radius of the splitting factor $\mathbb{L}_3$, which directly bounds the Taylor truncation error of the CP predictor (Section III). We therefore cap the diagonal at the polar rings by replacing $1/(1-u_1^2)$ and $1/(1-u_{N_u}^2)$ with the values of their inner neighbors, $1/(1-u_2^2)$ and $1/(1-u_{N_u-1}^2)$ [47]. This polar-cap regularization is consistent to the same order as the underlying second-order finite-difference scheme and is applied identically in the dense reference operator and in the CP factor matrices, so neither benchmark is biased by it.

The non-periodic second-difference matrix $\mathbf{D}_{\omega\omega} \in \mathbb{R}^{N_\omega \times N_\omega}$ in $\mathbb{L}_4$ is identical to the one used in the cylinder case [45],

$$\mathbf{D}_{\omega\omega} = \frac{1}{\Delta_\omega^2} \begin{bmatrix} -2 & 1 & 0 & 0 & 0 & 0 \\ 1 & -2 & 1 & 0 & 0 & 0 \\ 0 & 1 & -2 & 1 & 0 & 0 \\ 0 & 0 & \ddots & \ddots & \ddots & 0 \\ 0 & 0 & 0 & 1 & -2 & 1 \\ 0 & 0 & 0 & 0 & 1 & -2 \end{bmatrix} . \tag{22}$$

D. Diagonalizations

We now provide the eigendecompositions $\mathbf{A} = \mathbf{V}\mathbf{D}\mathbf{V}^{-1}$ of the twelve factor matrices in (17) that are required for the tensorized predictor. They are either circulant (closed-form Fourier eigenvectors), already diagonal (identities, $\mathrm{diag}(\underline{\omega})$, $\mathrm{diag}(1/(1-\underline{u}^2))$), or symmetric tridiagonal (numerical eigendecomposition computed once and stored).

The matrix $\mathbf{A}_{\varphi,1} = \mathbf{D}_\varphi$ is circulant and its eigendecomposition is identical to that in [45, Sec. II.D]: with $\gamma_\varphi = \exp\{2\pi\imath/N_\varphi\}$, where $\imath = \sqrt{-1}$, the eigenvectors and eigenvalues are

$$[\mathbf{V}_{\varphi,1}]_{i,j} = \frac{1}{\sqrt{N_\varphi}} \cdot \gamma_\varphi^{(i-1)(j-1)} , \tag{23}$$

$$\lambda_{\varphi,1,i} = \frac{1}{\Delta_\varphi} \sinh\!\left((i-1)\cdot\frac{2\pi\imath}{N_\varphi}\right) . \tag{24}$$

The matrix $\mathbf{A}_{\varphi,3} = \mathbf{D}_{\varphi\varphi}$ is also circulant and shares the same eigenvectors $\mathbf{V}_{\varphi,3} = \mathbf{V}_{\varphi,1}$, with eigenvalues

$$\lambda_{\varphi,3,i} = \frac{2}{\Delta_\varphi^2}\left(\cos\!\left((i-1)\cdot\frac{2\pi}{N_\varphi}\right) - 1\right) . \tag{25}$$

The remaining φ-factors $\mathbf{A}_{\varphi,2} = \mathbf{A}_{\varphi,4} = \mathbf{I}(N_\varphi)$ are trivially diagonal. Among the u-factors, $\mathbf{A}_{u,1} = \mathbf{A}_{u,4} = \mathbf{I}(N_u)$ are identities, and $\mathbf{A}_{u,3} = \mathrm{diag}\big(1/(1-\underline{u}^2)\big)$ is already diagonal. The remaining radial diffusion matrix $\mathbf{A}_{u,2} = \frac{q_n^2}{2}\mathbf{D}_u$ is a symmetric tridiagonal matrix with non-constant coefficients (and thus, unlike $\mathbf{D}_{\omega\omega}$, not Toeplitz). Its eigendecomposition is computed numerically once and stored. The eigenvalues are real and non-positive, and converge as $N_u \to \infty$ to those of the spherical Laplace-Beltrami operator's θ-part, $-\ell(\ell+1)$ for $\ell = 0, 1, 2, \ldots$. Among the ω-factors, $\mathbf{A}_{\omega,1} = -\,\mathrm{diag}(\underline{\omega})$ and $\mathbf{A}_{\omega,2} = \mathbf{A}_{\omega,3} = \mathbf{I}(N_\omega)$ are already diagonal. The matrix $\mathbf{A}_{\omega,4} = \frac{q_\omega^2}{2}\mathbf{D}_{\omega\omega}$ is the same symmetric Toeplitz matrix as in the cylinder case, whose eigendecomposition we compute numerically once and store, in agreement with [45, Sec. II.D].

III. Tensorized Prediction

The discretized FP equation in (11) is a linear Ordinary Differential Equation (ODE) system, formally solved by

$$\underline{p}(t+\tau) = \exp\{\tau\mathbb{L}\}\, \underline{p}(t) . \tag{26}$$

Since $\mathbb{L} \in \mathbb{R}^{N_\varphi N_u N_\omega \times N_\varphi N_u N_\omega}$, evaluating (26) naively, e.g., via a single dense matrix exponential or an off-the-shelf ODE solver on the full grid, becomes prohibitive for fine grids. We therefore directly reuse the tensorized predictor of [45], which exploits the Kronecker-sum structure of $\mathbb{L}$ in (17) together with a low-rank decomposition of $\underline{p}(t)$. With the first-order Lie-Suzuki-Trotter splitting [48], the matrix exponential factorizes as

$$\exp\{\tau\mathbb{L}\} = \prod_{k=1}^{4} \exp\{\tau\, \mathbf{A}_{\omega,k} \otimes \mathbf{A}_{u,k} \otimes \mathbf{A}_{\varphi,k}\} + \mathcal{O}(\tau^2) . \tag{27}$$

Compared to the cylinder case (two two-fold Kronecker factors), the splitting now involves four three-fold Kronecker factors, reflecting the additional spherical diffusion term and the additional state dimension. Each factor in (27) is evaluated using the eigendecompositions $\mathbf{A}_{*,k} = \mathbf{V}_{*,k}\mathbf{D}_{*,k}\mathbf{V}_{*,k}^{-1}$, exploiting that the matrix exponential of a Kronecker product of diagonalizable matrices is itself a Kronecker product [49],

$$\begin{aligned} &\exp\{\tau\, \mathbf{A}_{\omega,k} \otimes \mathbf{A}_{u,k} \otimes \mathbf{A}_{\varphi,k}\} \\ &\quad = (\mathbf{V}_{\omega,k} \otimes \mathbf{V}_{u,k} \otimes \mathbf{V}_{\varphi,k})\, \mathbf{E}_k \left(\mathbf{V}_{\omega,k}^{-1} \otimes \mathbf{V}_{u,k}^{-1} \otimes \mathbf{V}_{\varphi,k}^{-1}\right) \end{aligned} \tag{28}$$

where $\mathbf{E}_k = \exp\{\tau\, \mathbf{D}_{\omega,k} \otimes \mathbf{D}_{u,k} \otimes \mathbf{D}_{\varphi,k}\}$ is approximated via a Taylor series of order N_{T}, as in [45, Eq. 12]. Given a low-rank representation of the prior density

$$\underline{p}(t) = \sum_{l=1}^{L} \underline{\rho}_{\omega,l}(t) \otimes \underline{\rho}_{u,l}(t) \otimes \underline{\rho}_{\varphi,l}(t) , \tag{29}$$

each splitting step in (27) maps every loading-vector triple $(\underline{\rho}_{\omega,l}, \underline{\rho}_{u,l}, \underline{\rho}_{\varphi,l})$ to $N_{\mathrm{T}}+1$ new triples by independently transforming the three factors. After the four splitting steps of one prediction step of length τ, the rank grows from L to $L\cdot(N_{\mathrm{T}}+1)^4$, and truncation back to a target rank L' is applied to keep the representation compact. Unlike the cylinder case [45, Sec. III.C], where the matrix-shaped representation admitted

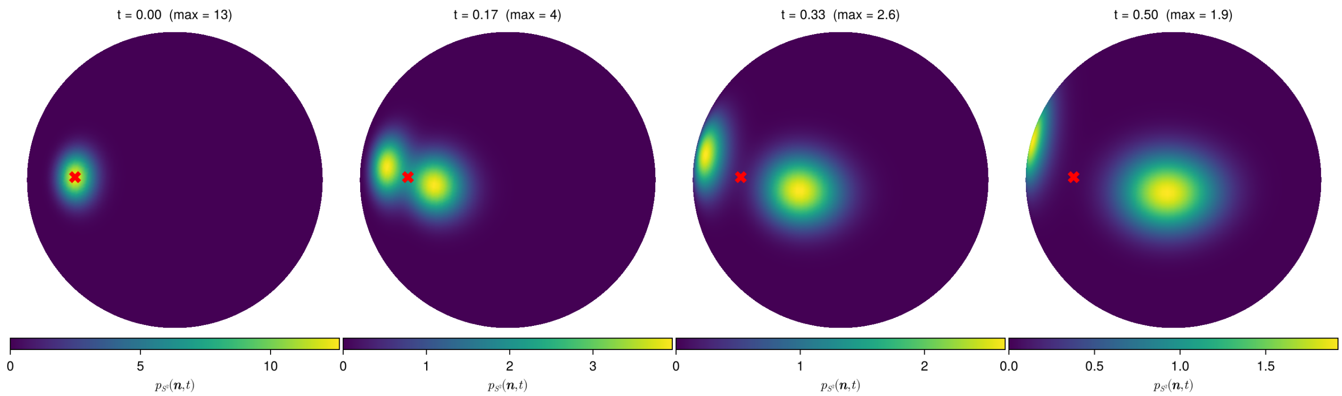

(a) Tsit5 predictor on the full grid

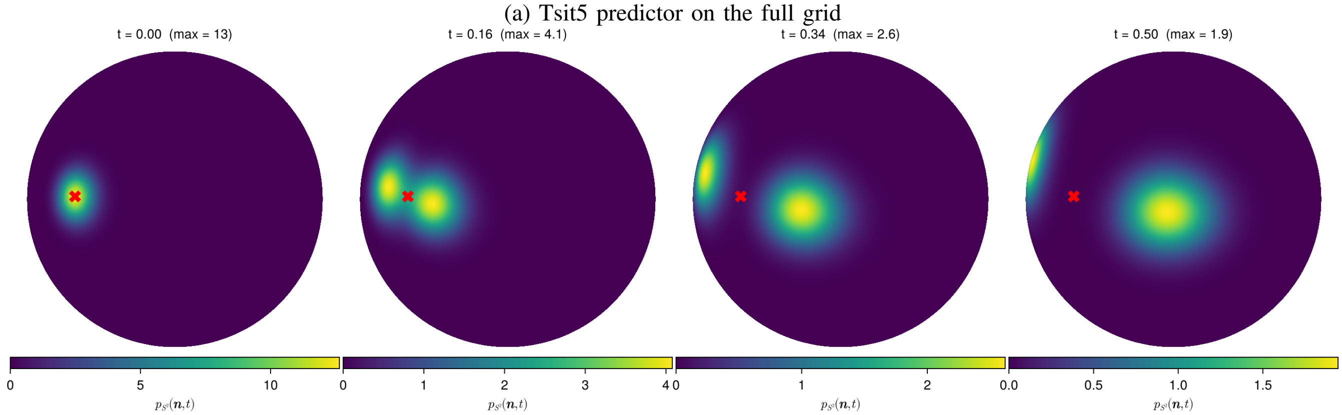

(b) CP predictor, proposed

Fig. 2: $\mathbb{S}^2$ marginal of the bimodal-ω scenario. (a): reference computed with the dense Tsit5 integrator on the full grid. (b): CP predictor with rank $L' = 4$, Taylor order $N_{\mathrm{T}} = 3$, and $N_{\mathrm{sub}} = 16$ sub-steps, on the same grid as (a). Each panel's colorbar is normalized to its own maximum. Red cross shows the initial mean direction for orientation.

a Singular Value Decomposition (SVD)-based truncation with its closed-form globally optimal solution, the present three-way tensor representation in (29) corresponds to a canonical polyadic decomposition, for which no analog of the SVD exists [38]. We therefore replace the SVD truncation by an Alternating Least Squares (ALS) update: keeping two of the three factor matrices fixed, the optimal third factor is the solution of a linear least-squares problem, and the three factors are updated cyclically until convergence. ALS is initialized from the L' leading rank-one terms of the inflated representation, which provides a good starting point and typically yields convergence within a few iterations. The choice of step size τ and Taylor order N_{T} trades single-step accuracy against the number of sub-steps required to reach a given prediction horizon, see [45, Sec. III.D].

The filter step can be performed according to [45, Sec. IV]. If the likelihood can be separated into φ and u, i.e., $\lambda(\varphi, u) = \lambda_\varphi(\varphi)\,\lambda_u(u)$, it is extremely simple: we just multiply the corresponding loading vectors by the likelihood factors. If the likelihood is a sum of multiple such terms, the rank will increase accordingly and we have to re-truncate with ALS. If the likelihood is non-separable, we first have to find a low-rank approximation [50].

IV. Evaluation

We evaluate the predictor on a bimodal scenario: the boresight $\underline{n}$ is concentrated about a reference direction $\underline{n}_0$, but the angular speed is equally likely to be $+\omega_0$ or $-\omega_0$. The initial density factorizes as

$$p_0(\underline{n}, \omega) \propto \exp(\kappa\, \underline{n}^\top \underline{n}_0) \cdot \left[\mathcal{N}(\omega; +\omega_0, \sigma_\omega^2) + \mathcal{N}(\omega; -\omega_0, \sigma_\omega^2)\right] \,, \tag{30}$$

i.e., a von Mises–Fisher (vMF) distribution on $\mathbb{S}^2$ times a Gaussian mixture with two components in ω. Numerically, we use $\kappa = 80$, $\underline{n}_0 = \underline{n}(u_0{=}0.3,\ \varphi_0{=}0)$, $\omega_0 = 1.5$, $\sigma_\omega = 0.3$, diffusion coefficients $q_n = 0.2$, $q_\omega = 0.15$, and prediction horizon $T = 0.5$. While the initial density is rank-1, this scenario turns into a stress test for the rank-L representation since the joint density becomes non-separable in $(\underline{n}, \omega)$ due to the velocity dependence on ω. The state space is discretized on the equispaced tensor grid of Section II-C with $N_\varphi = 160$, $N_u = 80$, $N_\omega = 81$, i.e., $\sim\!10^6$ unknowns; the truncation interval in ω is $[-3.5, 3.5]$. Since both Gaussian modes share the same spatial factor, the joint density factorizes as $p_0(\underline{n}, \omega) = S(\underline{n})\, G(\omega)$, and the ω-mixture collapses into a single loading vector $G(\omega) = \frac{1}{2}[\mathcal{N}(+\omega_0) + \mathcal{N}(-\omega_0)]$. Combined with a thin SVD of the spatial vMF factor S (cutoff 10^{-10}, retaining r_S singular values), this yields

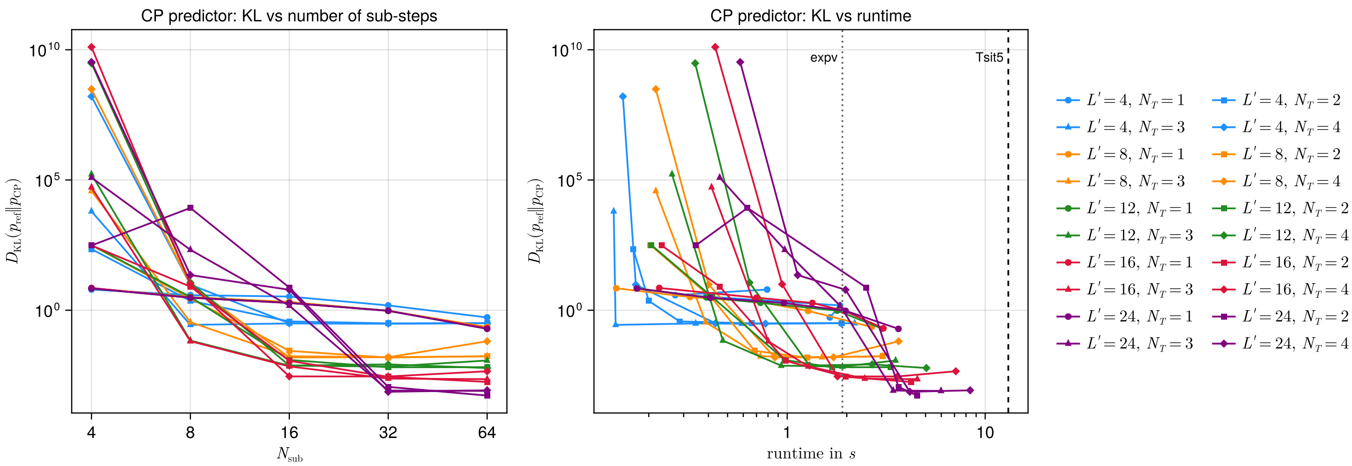

Fig. 3: Parameter sweep of the CP predictor on the bimodal-ω scenario. Left: divergence between the CP predictor and the Tsit5 reference as a function of the number of sub-steps N_{sub}. Right: divergence vs. wall-clock runtime; the dashed and dotted vertical lines mark the runtimes of the dense Tsit5 and Krylov `expv` reference solvers on the same grid.

an exact initial CP decomposition of rank r_S. Two dense baselines serve as references: the adaptive Runge–Kutta integrator *Tsit5* from `DifferentialEquations.jl` [51] (tolerances $10^{-9}/10^{-7}$) and the Krylov matrix-exponential routine `expv` from `ExponentialUtilities.jl` (tolerance 10^{-8}, Krylov dimension 30). Both operate on the full sparse $\mathbb{L}$ and would become prohibitive in higher state-space dimensions; here they provide a ground truth for the same operator. As error metric we use the discrete generalized Kullback–Leibler divergence (I-divergence)

$$D_{\text{KL}}(p_{\text{ref}} \,\|\, p_{\text{CP}}) = \sum_{i,j,m} \left[p_{\text{ref}} \log \frac{p_{\text{ref}}}{p_{\text{CP}}} - p_{\text{ref}} + p_{\text{CP}} \right] \Delta_u \, \Delta_\varphi \, \Delta_\omega \ , \tag{31}$$

which is well-defined without normalization and additionally penalizes any mass loss or gain in the predictor output. Figures 2a and 2b compare the dense Tsit5 reference and the CP predictor (rank $L' = 4$, Taylor order $N_{\text{T}} = 3$, $N_{\text{sub}} = 16$ sub-steps) at four equispaced times in $[0, T]$. The two are visually indistinguishable on the $\mathbb{S}^2$ marginal. Complementary to the spatial $\mathbb{S}^2$ marginal, Fig. 4 shows the time evolution of the ω-marginal $p_\omega(\omega, t) = \int_{\mathbb{S}^2} p(\underline{n}, \omega, t) \, \mathrm{d}\underline{n}$ of the dense reference. Starting from the symmetric two-mode Gaussian mixture at $t = 0$, the ω-diffusion progressively broadens the two peaks and would eventually merge them, while the total mass and the even symmetry about $\omega = 0$ are preserved throughout the prediction horizon.

Figure 3 sweeps the predictor parameters $L' \in \{4, 8, 12, 16, 24\}$, $N_{\text{T}} \in \{1, 2, 3, 4\}$, and $N_{\text{sub}} \in \{4, 8, 16, 32, 64\}$. The left panel shows the I-divergence at $t = T$ as a function of the number of sub-steps, the right panel as a function of wall-clock runtime, with the dense Tsit5 and `expv` runtimes indicated as vertical reference lines. Increasing L' reduces the truncation floor; increasing N_{T} accelerates convergence in τ at fixed L' until the truncation floor is hit. For moderate accuracy ($D_{\text{KL}} \sim 10^{-3}$), the CP predictor is an order of magnitude faster than the dense

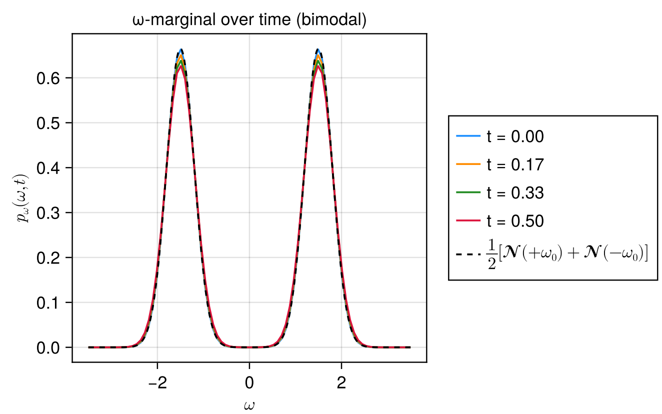

Fig. 4: Time evolution of the ω-marginal $p_\omega(\omega, t)$ for the bimodal-ω scenario, obtained from the dense Tsit5 reference. The dashed curve is the initial symmetric Gaussian mixture $\frac{1}{2}[\mathcal{N}(+\omega_0) + \mathcal{N}(-\omega_0)]$; the colored curves show the slight ω-diffusion broadening over time, while preserving total mass and the symmetry about $\omega = 0$.

baselines, and its advantage grows with the grid size since the per-step cost scales only with the mode sizes rather than with the full $N_\varphi N_u N_\omega$. Note that the method can produce slightly negative and also complex numbers. Dealing with this, e.g., via a square root representation, is future work.

Julia source code is supplied on CodeOcean[1] and linked on the IEEE Xplore page.

V. Conclusion

We presented a low-rank FP predictor for the joint density of a pointing direction and its unknown rotation speed on the product manifold $\mathbb{S}^2 \times \mathbb{R}$, fully accounting for the curvature and periodicity of the sphere. The equal-area $u = \cos\theta$ parametrization turns the spherical Laplace-Beltrami diffusion into a regular Sturm-Liouville operator

[1] `https://codeocean.com/capsule/7007445/tree`

free of polar singularities, and the resulting Kronecker-sum structure of the discretized operator carries over directly to the tensorized predictor. By replacing the matrix representation of the cylinder case with a three-way canonical polyadic decomposition and an alternating-least-squares truncation, we predict densities on the sphere accurately while tying the per-step cost to the individual mode sizes rather than to the full grid. On a bimodal angular-speed scenario, the predictor reproduced dense reference solvers to high accuracy at an order-of-magnitude lower runtime – a margin that widens as the grid is refined – and captured the strong coupling between the directional and angular-speed components with only a few loading vectors. The approach extends naturally to other system dynamics and to further Riemannian manifolds and their Cartesian products with Euclidean spaces, such as the torus, hypertori, and the rigid-body groups $\mathrm{SE}(2)$ and $\mathrm{SE}(3)$.

References

[1] Dalton Durant, Uwe D. Hanebeck, and Renato Zanetti. "Good Things Come to Those Who Weight! Improving Gaussian Mixture Weights for Cislunar Debris Tracking". In: *Proceedings of the AAS/AIAA Space Flight Mechanics Meeting, Kaua'i, Hawaii*. 25. Kaua'i, Hawaii, Jan. 2025, p. 309.

[2] Weixin Wang and Taeyoung Lee. *Matrix Fisher-Gaussian Distribution on SO(3) x R^n for Attitude Estimation with a Gyro Bias*. May 2020. DOI: 10.48550/arXiv.2003.02180. (Visited on 04/13/2026).

[3] Daniel Frisch and Uwe D. Hanebeck. "The Generalized Fibonacci Grid as Low-Discrepancy Point Set for Optimal Deterministic Gaussian Sampling". In: *Journal of Advances in Information Fusion* 18.1 (June 2023), pp. 16–34. URL: https://isif.org/media/generalized-fibonacci-grid-low-discrepancy-point-set-optimal-deterministic-gaussian-sampling.

[4] Daniel Frisch and Uwe D. Hanebeck. "Deterministic Gaussian Sampling With Generalized Fibonacci Grids". In: *Proceedings of the 24th International Conference on Information Fusion (Fusion 2021)*. Sun City, South Africa, Nov. 2021. DOI: 10.23919/FUSION49465.2021.9626975.

[5] Jannik Steinbring, Martin Pander, and Uwe D. Hanebeck. "The Smart Sampling Kalman Filter with Symmetric Samples". In: *Journal of Advances in Information Fusion* 11.1 (June 2016), pp. 71–90. URL: https://isif.org/media/smart-sampling-kalman-filter-symmetric-samples.

[6] Daniel Frisch and Uwe D. Hanebeck. "Gaussian Mixture Particle Filter Step based on Method of Moments". In: *Proceedings of the 27th International Conference on Information Fusion (FUSION 2024)*. Venice, Italy, July 2024. DOI: 10.23919/FUSION59988.2024.10706458.

[7] Daniel Frisch and Uwe D. Hanebeck. "Gaussian Mixture Estimation from Weighted Samples". In: *Proceedings of the 2021 IEEE International Conference on Multisensor Fusion and Integration for Intelligent Systems (MFI 2021)*. Karlsruhe, Germany, Sept. 2021. DOI: 10.1109/MFI52462.2021.9591161.

[8] Daniel Frisch and Uwe D. Hanebeck. "Deterministic Sampling on the Circle Using Projected Cumulative Distributions". In: *Proceedings of the 25th International Conference on Information Fusion (Fusion 2022)*. Linköping, Sweden, July 2022. DOI: 10.23919/FUSION49751.2022.9841299.

[9] Vlad M. Korsakov, Daniel Frisch, and Uwe D. Hanebeck. "Deterministic Sampling of the Watson Distribution". In: *Proceedings of the 29th International Conference on Information Fusion (FUSION 2026)*. Trondheim, Norway, June 2026.

[10] Daniel Frisch and Uwe D. Hanebeck. "Deterministic Sampling with Separation of Variables in Spherical Coordinates". In: *Proceedings of the 28th International Conference on Information Fusion (FUSION 2025)*. Rio de Janeiro, Brazil, July 2025. DOI: 10.23919/FUSION65864.2025.11124009.

[11] Daniel Frisch and Uwe D. Hanebeck. "Deterministic Von Mises-Fisher Sampling on the Sphere Using Fibonacci Lattices". In: *Proceedings of the combined IEEE 2023 Symposium Sensor Data Fusion and International Conference on Multisensor Fusion and Integration (SDF-MFI 2023)*. Bonn, Germany, Nov. 2023. DOI: 10.1109/SDF-MFI59545.2023.10361396.

[12] Kailai Li, Florian Pfaff, and Uwe D. Hanebeck. "Hyperspherical Dirac Mixture Reapproximation". In: *arXiv preprint arXiv:2110.10411* (Oct. 2021). DOI: 10.48550/arXiv.2110.10411.

[13] Daniel Frisch, Kailai Li, and Uwe D. Hanebeck. "Optimal Reduction of Dirac Mixture Densities on the 2-Sphere". In: *Proceedings of the 1st Virtual IFAC World Congress (IFAC-V 2020)*. July 2020. DOI: 10.1016/j.ifacol.2020.12.1856.

[14] Gerhard Kurz and Uwe D. Hanebeck. "Deterministic Sampling on the Torus for Bivariate Circular Estimation". In: *IEEE Transactions on Aerospace and Electronic Systems* 53.1 (Feb. 2017), pp. 530–534. DOI: 10.1109/TAES.2017.2650079.

[15] Gerhard Kurz, Florian Pfaff, and Uwe D. Hanebeck. "Nonlinear Toroidal Filtering Based on Bivariate Wrapped Normal Distributions". In: *Proceedings of the 20th International Conference on Information Fusion (Fusion 2017)*. Xi'an, China, July 2017. DOI: 10.23919/ICIF.2017.8009831.

[16] Gerhard Kurz and Uwe D. Hanebeck. "Toroidal Information Fusion Based on the Bivariate von Mises Distribution". In: *Proceedings of the 2015 IEEE International Conference on Multisensor Fusion and Integration for Intelligent Systems (MFI 2015)*. San Diego, California, USA, Sept. 2015. DOI: 10.1109/MFI.2015.7295826.

[17] Gerhard Kurz, Igor Gilitschenski, and Uwe D. Hanebeck. "The Partially Wrapped Normal Distribution for SE(2) Estimation". In: *Proceedings of the 2014 IEEE International Conference on Multisensor Fusion and Information Integration (MFI 2014)*. Beijing, China, Sept. 2014. DOI: 10.1109/MFI.2014.6997733.

[18] Kailai Li, Gerhard Kurz, Lukas Bernreiter, and Uwe D. Hanebeck. "Nonlinear Progressive Filtering for SE(2) Estimation". In: *Proceedings of the 21st International Conference on Information Fusion (Fusion 2018)*. Cambridge, United Kingdom, July 2018. DOI: 10.23919/ICIF.2018.8455231.

[19] Kailai Li, Florian Pfaff, and Uwe D. Hanebeck. "Unscented Dual Quaternion Particle Filter for SE(3) Estimation". In: *IEEE Control Systems Letters* 5.2 (2021), pp. 647–652. DOI: 10.1109/LCSYS.2020.3005066.

[20] Kailai Li, Florian Pfaff, and Uwe D. Hanebeck. "Geometry-Driven Stochastic Modeling of SE(3) States Based on Dual Quaternion Representation". In: *Proceedings of the 2019 IEEE International Conference on Multisensor Fusion and Integration for Intelligent Systems (MFI 2019), part of 2019 IEEE International Conference on Industrial Cyber Physical Systems (ICPS 2019)*. Taipei, Republic of China, May 2019. DOI: 10.1109/ICPHYS.2019.8780254.

[21] Søren Hauberg, François Lauze, and Kim Steenstrup Pedersen. "Unscented Kalman Filtering on Riemannian Manifolds". In: *Journal of Mathematical Imaging and Vision* 46.1 (May 2013), pp. 103–120.

[22] Uwe D. Hanebeck and Martin Pander. "Progressive Bayesian Estimation with Deterministic Particles". In: *Proceedings of the 19th International Conference on Information Fusion (Fusion 2016)*. Heidelberg, Germany, July 2016. URL: https://ieeexplore.ieee.org/document/7528132.

[23] Uwe D. Hanebeck. "Progressive Bayesian Particle Flows Based on Optimal Transport Map Sequences". In: *Proceedings of the 26th International Conference on Information Fusion (Fusion 2023)*. Charleston, USA, June 2023. DOI: 10.23919/FUSION52260.2023.10224077.

[24] Sukkeun Kim and Uwe D. Hanebeck. "The Hitchhiker's Guide to Particle Flow-based Filters: A Survey". In: *Proceedings of the 23rd IFAC World Congress (IFAC 2026)*. Busan, Republic of Korea, Aug. 2026.

[25] Sukkeun Kim and Uwe D. Hanebeck. "Deterministic Prior Sample Set Prediction Approaches for Newton-Flow Particle Filters". In: *Proceedings of the 29th International Conference on Information Fusion (FUSION 2026)*. Trondheim, Norway, June 2026.

[26] Uwe D. Hanebeck. "Newton-Flow Particle Filters based on Generalized Cramér Distance". In: *arXiv preprint: 2509.00182* (Aug. 2025). DOI: 10.48550/arXiv.2509.00182.

[27] Miroslav Simandl, Jakub Královec, and Torsten Söderström. "Advanced Point-Mass Method for Nonlinear State Estimation". In: *Automatica* 42.7 (2006), pp. 1133–1145. DOI: 10.1016/j.automatica.2006.03.010.

[28] H. Zhang and D. Laneuville. "Grid Based Solution of Zakai Equation with Adaptive Local Refinement for Bearings-only Tracking". In: *2008 IEEE Aerospace Conference*. 2008, pp. 1–8. DOI: 10.1109/AERO.2008.4526436.

[29] Felipe Giraldo Grueso, Andrey A. Popov, Uwe D. Hanebeck, and Renato Zanetti. "Optimal Sampling for Point Mass Filtering with Applications to Cislunar Orbit Determination". In: *The Journal of the Astronautical Sciences* (2025), pp. 1–34. DOI: 10.1007/s40295-025-00521-7.

[30] Florian Pfaff, Kailai Li, and Uwe D. Hanebeck. "Fourier Filters, Grid Filters, and the Fourier-Interpreted Grid Filter". In: *Proceedings of the 22nd International Conference on Information Fusion (Fusion 2019)*. Ottawa, Canada, July 2019. DOI: 10.23919/FUSION43075.2019.9011318.

[31] Florian Pfaff, Kailai Li, and Uwe D. Hanebeck. "Conditional Densities and Likelihoods for Hypertoroidal Densities Based on Trigonometric Polynomials". In: *Proceedings of the 2021 IEEE International Conference on Multisensor Fusion and Integration for Intelligent Systems (MFI 2021)*. Karlsruhe, Germany, Sept. 2021. DOI: 10.1109/MFI52462.2021.9591160.

[32] Florian Pfaff, Kailai Li, and Uwe D. Hanebeck. "Estimating Correlated Angles Using the Hypertoroidal Grid Filter". In: *Proceedings of the 2020 IEEE International Conference on Multisensor Fusion and Integration for Intelligent Systems (MFI 2020)*. Virtual, Sept. 2020. DOI: 10.1109/MFI49285.2020.9235220.

[33] Florian Pfaff, Kailai Li, and Uwe D. Hanebeck. "The Spherical Grid Filter for Nonlinear Estimation on the Unit Sphere". In: *Proceedings of the 1st Virtual IFAC World Congress (IFAC-V 2020)*. July 2020. DOI: 10.1016/j.ifacol.2020.12.031.

[34] Florian Pfaff, Kailai Li, and Uwe D. Hanebeck. "A Hyperhemispherical Grid Filter for Orientation Estimation". In: *Proceedings of the 23rd International Conference on Information Fusion (Fusion 2020)*. Virtual, July 2020. DOI: 10.23919/FUSION45008.2020.9190611.

[35] Kailai Li, Florian Pfaff, and Uwe D. Hanebeck. "Grid-Based Quaternion Filter for SO(3) Estimation". In: *Proceedings of the 2020 European Control Conference (ECC 2020)*. Virtual, May 2020. DOI: 10.23919/ECC51009.2020.9143723.

[36] Gerhard Kurz, Florian Pfaff, and Uwe D. Hanebeck. "Discretization of SO(3) Using Recursive Tesseract Subdivision". In: *Proceedings of the 2017 IEEE International Conference on Multisensor Fusion and Integration for Intelligent Systems (MFI 2017)*. Daegu, Republic of Korea, Nov. 2017. DOI: 10.1109/MFI.2017.8170406.

[37] Florian Pfaff, Kailai Li, and Uwe D. Hanebeck. "The State Space Subdivision Filter for SE(3)". In: *Proceedings of the 25th International Conference on Information Fusion (Fusion 2022)*. Linköping, Sweden, July 2022. DOI: 10.23919/FUSION49751.2022.9841384.

[38] Tamara G. Kolda and Brett W. Bader. "Tensor Decompositions and Applications". In: *SIAM Review* 51.3 (2009), pp. 455–500. DOI: 10.1137/07070111X.

[39] Frank L. Hitchcock. "The Expression of a Tensor or a Polyadic as a Sum of Products". In: *Journal of Mathematics and Physics* 6.1-4 (1927), pp. 164–189. DOI: 10.1002/sapm192761164.

[40] Bruno Demissie, Muhammad Altamash Khan, and Felix Govaers. "Nonlinear Filter Design Using Fokker-Planck Propagator in Kronecker Tensor Format". In: *2016 19th International Conference on Information Fusion (FUSION)*. 2016, pp. 1–8.

[41] Muhammad Altamash Khan, Martin Ulmke, Bruno Demissie, Felix Govaers, and Wolfgang Koch. "Combining Log-Homotopy Flow With Tensor Decomposition Based Solution for Fokker-Planck Equation". In: *2016 19th International Conference on Information Fusion (FUSION)*. 2016, pp. 2229–2236.

[42] Felix Govaers, Bruno Demissie, Altamash Khan, Martin Ulmke, and Wolfgang Koch. "Tensor Decomposition-Based Multitarget Tracking in Cluttered Environments". In: *Journal of Advances in Information Fusion* 14.1 (2019), p. 86. URL: https://isif.org/media/tensor-decomposition-based-multitarget-tracking-cluttered-environments.

[43] Jakub Matousek, Jan Krejci, Jindrich Dunik, and Renato Zanetti. *Tensor Decompositions for Online Grid-Based Terrain-Aided Navigation*. 2026. URL: https://arxiv.org/abs/2601.07728.

[44] Daniel Frisch and Uwe D. Hanebeck. "Interpolation of Probability Densities on a Grid in Tensor Decomposition Representation". In: *Proceedings of the 29th International Conference on Information Fusion (FUSION 2026)*. Trondheim, Norway, June 2026.

[45] Daniel Frisch and Uwe D. Hanebeck. "Fokker-Planck Prediction on the Cylindric Manifold using Tensor Decomposition of a Regular Grid". In: *17th Symposium Sensor Data Fusion: Trends, Solutions, Applications (SDF 2025)*. Bonn, Germany, Nov. 2025. DOI: 10.1109/SDF67080.2025.11330240.

[46] Elton Hsu. "Stochastic Analysis on Manifolds". In: vol. 38. Graduate Studies in Mathematics. Providence, Rhode Island: American Mathematical Society, Feb. 2002. DOI: 10.1090/gsm/038. (Visited on 06/02/2026).

[47] Kamran Mohseni and Tim Colonius. "Numerical Treatment of Polar Coordinate Singularities". In: *Journal of Computational Physics* 157.2 (Jan. 2000), pp. 787–795. DOI: 10.1006/jcph.1999.6382. (Visited on 06/05/2026).

[48] Masuo Suzuki. "Fractal Decomposition of Exponential Operators with Applications to Many-Body Theories and Monte Carlo Simulations". In: *Physics Letters A* 146.6 (1990), pp. 319–323. DOI: 10.1016/0375-9601(90)90962-N.

[49] Charles F. Van Loan. "The Ubiquitous Kronecker Product". In: *Journal of Computational and Applied Mathematics* 123.1 (2000), pp. 85–100. DOI: 10.1016/S0377-0427(00)00393-9.

[50] Felix Govaers and Joshua Gehlen. "Rank-1 Decomposition for Grid-Based Likelihood Functions of Measurements in Polar Coordinates". In: *Proceedings of the 29th International Conference on Information Fusion (FUSION 2026)*. Trondheim, Norway, June 2026.

[51] Christopher Rackauckas and Qing Nie. "DifferentialEquations.Jl–a Performant and Feature-Rich Ecosystem for Solving Differential Equations in Julia". In: *Journal of Open Research Software* 5.1 (2017). DOI: 10.5334/jors.151.